On the pH-Modulated Ru-Based Prodrug Activation Mechanism

Marco Caterino,[†,§] Mona Herrmann,[‡,§] Antonello Merlino,[†] Claudia Riccardi,[†]
Daniela Montesarchio,[†] Maria A. Mroginski,[‡] Domenica Musumeci,[†] Francesco Ruffo,[†]
Luigi Paduano,[†] Peter Hildebrandt,[‡] Jacek Kozuch,[*,‡,⊥] and Alessandro Vergara[*,†,∥]

[†]Department of Chemical Sciences, University of Naples Federico II, via Cinthia, Naples I-80126, Italy
[‡]Institut für Chemie, Technische Universität Berlin, Straße des 17 Juni 135, Berlin 10623, Germany
[∥]CEINGE, Biotecnologie Avanzate s.c.a.r.l.m., via G Salvatore, Naples I-80131, Italy

S Supporting Information

ABSTRACT: The Ru^{III}-based prodrug AziRu efficiently binds to proteins, but the mechanism of its release is still disputed. Herein, in order to test the hypothesis of a reduction-mediated Ru release from proteins, a Raman-assisted crystallographic study on AziRu binding to a model protein (hen egg white lysozyme), in two different oxidation states, Ru^{II} and Ru^{III}, was carried out. Our results indicate Ru reduction, but the Ru release upon reduction is dependent on the reducing agent. To better understand this process, a pH-dependent, spectroelectrochemical surface-enhanced Raman scattering (SERS) study was performed also on AziRu-functionalized Au electrodes as a surrogate and simplest model system of Ru^{II}- and Ru^{III}-based drugs. This SERS study provided a pK_a of 6.0 ± 0.4 for aquated AziRu in the Ru^{III} state, which falls in the watershed range of pH values separating most cancer environments from their physiological counterparts. These experiments also indicate a dramatic shift of the redox potential E_0 by >600 mV of aquated AziRu toward more positive potentials upon acidification, suggesting a selective AziRu reduction in cancer lumen but not in healthy ones. It is expected that the nature of the ligands (e.g., pyridine vs imidazole, present in well-known Ru^{III} complex NAMI-A) will modulate the pK_a and E_0, without affecting the underlying reaction mechanism.
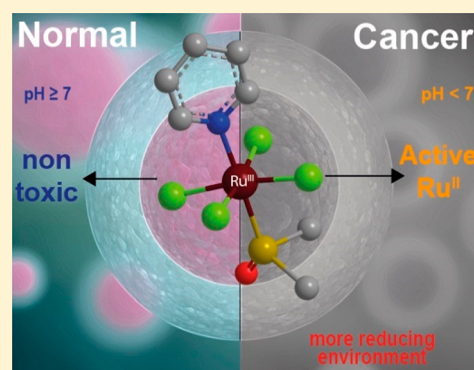
INTRODUCTION

The effectiveness of an anticancer drug goes far beyond its mere cytotoxic or antiproliferative activities. The utmost pressing and trending topic in the current drug design course is selectivity, meant as a whole of pharmacological facets, making a drug capable of picking out malignant targets and avoiding unwanted impact on healthy cells. To this end, cancer conditions exhibit various sizeably different chemical features compared to healthy ones, which can thus be exploited as target labeling features. The high proliferation rate of transformed cancer cells prompts a severe increase of hypoxia metabolism and therefore an extracellular lumen pH acidification as low as 6 compared to the physiological pH 7.4.[1] In addition, the tumor invariably progresses, hindering the reactive oxygen species processing ability and giving rise to a more radical-rich reducing environment.[2]

The last decades witnessed a significant increase in the design of new Ru-based complexes, proven to be effective as anticancer agents.[3] Much of their success in the current anticancer panorama is due to the ease with which they access multiple oxidation states under physiological conditions, although their mechanisms of action remain not completely understood.[3,4] Ru^{III} is the prevailing, most stable but marginally anticancer active form, largely bound to blood-plasma proteins once administered, essentially acting as a prodrug.[5−7] Antitumor potential has been proven to rely on the reduction to Ru^{II},[5−12] which can be promptly accessed in the presence of ordinary biological reducing agents, particularly abundant within cancer environments, opening the perspective for possible *selective drug activation*.[6−8,10,13−15]

Many Ru^{III}-based complexes have recently been proposed, and although none of them has reached actual clinical usage as of yet, two acclaimed complexes introduced roughly at the same time, namely, NAMI-A and KP1019, have both entered clinical trials.[16,17]

The subject of this study is the recently proposed $Na^+[trans\text{-}RuCl_4(1H\text{-}Pyr)(DMSO\text{-}S)]$ complex (AziRu; Figure 1, right),[18−20] whose structure differs from NAMI-A by a pyridine ring in place of an imidazole moiety.[3,5,21] AziRu has proven to have promising activity and has thus been selected to obtain a focused library of highly antiproliferative nucleolipid-decorated Ru^{III} complexes.[20,22−24]

The combination of X-ray crystallography and Raman microspectroscopy provided fundamental structural insight into the interaction with two model proteins, RNase A and lysozyme, and shed light on the ligand-exchange process.[25,26] Indeed, Raman assistance in crystallographic studies has been
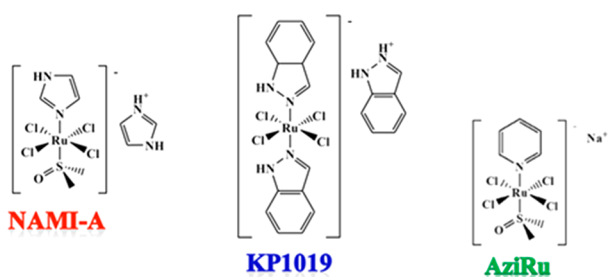
Figure 1. Molecular structures of the Ru^{III} complexes NAMI-A, KP1019, and AziRu.

proven to disentangle ambiguities in protein−metal interaction not only for heme proteins[27−29] but also for several metals other than Ru.[30−33] Furthermore, the information obtained from Raman spectroscopy on crystals can be readily compared with spectroelectrochemical studies in the condensed phase or at model surfaces where conditions such as the pH or electrochemical potential can be controlled very efficiently.[34]

This study brings Raman-assisted crystallographic clues for chemical-reduction-dependent Ru release from the model protein hen egg white lysozyme (HEWL) as well as surface-enhanced Raman spectroscopy (SERS) investigations to grasp whether AziRu is compatible with a selective pH- and/or reduction-potential-related activation within cancerous environments.

■ EXPERIMENTAL SECTION

Materials and General Methods. All of the reagents and solvents were of the highest commercially available quality and were used as received. Thin-layer chromatography (TLC) analyses were carried out on silica gel plates from Macherey-Nagel (60, F254). Reaction products on TLC plates were visualized by UV light and then by treatment with an oxidant acidic solution [10:4:5 (v/v) acetic acid/H$_2$O/sulfuric acid (H$_2$SO$_4$)]. NMR spectra were recorded on Bruker WM-400 and Varian Inova 500 spectrometers, as specified. All of the *chemical shifts* (δ) are expressed in ppm with respect to the residual solvent signal for both ^{1}H NMR [CDCl$_3$, 7.26 ppm; DMSO-d_6, 2.50 ppm] and ^{13}C NMR (CDCl$_3$, 76.9 ppm). All of the coupling constants (J) are quoted in Hertz (Hz). The following abbreviations were used to explain the multiplicities: s = singlet; d = doublet; t = triplet; q = quartet; m = multiplet; b = broad. Matrix-assisted laser desorption/ionization time-of-flight (MALDI-TOF) mass spectrometry (MS) analyses were performed on a TOF/TOF 5800 system in the positive mode, using 2,5-dihydroxybenzoic acid (DHB) as the matrix. For deposition on the MALDI plate, the droplet spotting method was used: the sample (1 μg μL^{-1}) in 7:3 (v/v) acetonitrile (CH$_3$CN)/methanol (MeOH) was first deposited on the plate followed by DHB deposition [10 mg mL^{-1} in 7:3 (v/v) CH$_3$CN/MeOH] with proper mixing before drying the components. The MS spectra were recorded in the m/z 100−1000 range. Electrospray ionization MS (ESI-MS) analyses were performed on an Agilent 6230B TOF liquid chromatography (LC)/MS instrument, equipped with an electrospray source. Stock solutions of the samples were prepared at 1 mg mL^{-1} concentration in CH$_3$CN/water (H$_2$O), high-performance liquid chromatography (HPLC) grade (1:1, v/v). Direct injections were carried out at a final concentration of 4 μg μL^{-1}, acquiring the ESI-MS spectra in positive-ion mode in the m/z 300−1100 range. The UV−vis measurements were performed on a Jasco V-530 UV−vis spectrophotometer equipped with a Peltier Jasco ETC-505T thermostat by using 1-cm-path length cuvette. The spectra were recorded at room temperature in the 200−600 nm range with a medium response, a scanning speed of 100 nm min^{-1}, and a 2.0 nm bandwidth with the appropriate baseline subtracted. All of the spectra were averaged over three scans, and each experiment was performed in triplicate. All of the target compounds were analyzed from samples

freshly dissolved at 100 μM concentration in CH$_3$CN. IR spectra were obtained on a Jasco FTIR-4100 spectrometer in the 4000−400 cm^{-1} range.

Synthesis of 2-(Pyridin-4-yl)ethanethiol (PySH). Commercially available 2-(4-pyridinyl)ethanethiol hydrochloride (502 mg, 2.86 mmol) and sodium hydroxide (NaOH; 114 mg, 2.86 mmol) were dissolved in 13 mL of MeOH and then left under stirring at room temperature. The reaction, monitored by pH measurements, was quenched after ca. 30 min by solvent removal under reduced pressure, and the crude product was extracted with dichloromethane (CH$_2$Cl$_2$)/H$_2$O. The desired compound was recovered in the organic phases, which were dried upon the addition of anhydrous sodium sulfate (Na$_2$SO$_4$), filtered, and concentrated under reduced pressure. The pure compound, here indicated as PySH (Scheme S1), was obtained in 82% isolated yield (327 mg, 2.35 mmol).

PySH. Yellow oil. R_f = 0.8 [8:2 (v/v) CH$_2$Cl$_2$/MeOH]. ^{1}H NMR (500 MHz, CDCl$_3$): δ 8.52 (d, J = 5.5 Hz, 2H, 2 × $H\alpha$ Py), 7.12 (d, J = 5.5 Hz, 2H, 2 × $H\beta$ Py), 2.91 (t, J = 7.5 Hz, 2H, CH$_2$CH$_2$SH), 2.79 (q, 2H, CH$_2$SH), 1.38 (t, J = 8.0 Hz 1H, SH). ^{13}C NMR (125 MHz, CDCl$_3$): δ 149.8 (2 × $C\alpha$ Py), 148.3 ($C\gamma$ Py), 123.8 (2 × $C\beta$ Py), 39.2 (CH$_2$CH$_2$SH), 24.6 (CH$_2$SH).

Synthesis of 1,2-Bis[2-(pyridin-4-yl)ethyl]disulfane (PySS-Py). Pure PySH (100 mg, 0.72 mmol) was dissolved in 500 μL of MeOH, and then hydrogen peroxide (H$_2$O$_2$; 90 μL of a 30 wt % H$_2$O solution, 0.80 mmol) and KI (11.6 mg, 0.07 mmol) were sequentially added to the reaction mixture, left under stirring at room temperature. After 1 h, TLC analysis indicated the appearance of a new product with the concomitant disappearance of the starting material. The reaction was thus quenched by the addition of a few drops of H$_2$O, the solvent was removed in vacuo, and the crude product was extracted with CH$_2$Cl$_2$/H$_2$O. The desired compound was recovered in the organic phase, which was dried over anhydrous Na$_2$SO$_4$, filtered, and then taken to dryness, giving compound PySSPy in almost quantitative yield (98.0 mg, 0.35 mmol).

PySSPy. Yellow oil. R_f = 0.6 (CH$_2$Cl$_2$/MeOH, 95:5, v/v). ^{1}H NMR (400 MHz, CDCl$_3$; Figure S1): δ 8.50 (d, J = 5.5 Hz, 4H, 2 × Hα Py), 7.10 (d, J = 5.5 Hz, 4H, 2 × Hβ Py), 2.99−2.89 (m, 8H, 2 × CH$_2$CH$_2$S). ^{13}C NMR (100 MHz, CDCl$_3$; Figure S2): δ 149.7 (2 × Cα Py), 148.3 (2 × Cγ Py), 123.8 (2 × Cβ Py), 38.4 (CH$_2$CH$_2$SH), 34.5 (CH$_2$SH). MALDI-MS (positive ions; Figure S3). Mass calcd for C$_{14}$H$_{16}$N$_2$S$_2$ [M]: m/z 276.08. Found: m/z 276.86 [M + H$^+$], 298.89 [M + Na$^+$], 314.94 [M + K$^+$]. IR (Figure S7; ν_{max}, cm^{-1}): 3500−3000 (s) [C−H], 1595 (s), 1557 (m) [C=N], 1416 (s), 1215 (m), 991 (m) [CH$_2$], 798 (s) [C−S], 575 (m), 500 (m) [S−S].

Synthesis of RuPySSPyRu. Pure PySSPy (10.0 mg, 0.04 mmol) was dissolved in 10 mL of dry acetone, and then Na$^+$[*trans*-RuCl$_4$(DMSO)$_2$]$^-$ (25.3 mg, 0.06 mmol), synthesized according to previous protocols,[35] was added to the reaction mixture and left under stirring at room temperature. After 2 h, TLC monitoring indicated the complete disappearance of both starting materials and the formation of a new product. The desired Ru complex RuPySSPyRu was recovered in 75% isolated yield (28.9 mg, 0.03 mmol) by solvent removal under vacuum, followed by precipitation in CH$_2$Cl$_2$.

RuPySSPyRu. Orange, amorphous powder. R_f = 0.3 [85:15 (v/v) CH$_2$Cl$_2$/MeOH]. ^{1}H NMR (400 MHz, DMSO-d_6; Figure S4): significant signals at δ −2.40 (very broad signal, Py protons), −13.0 (very broad signal, CH$_3$ of DMSO). ESI-MS (positive ions; Figure S5). Calcd for C$_{18}$H$_{28}$Cl$_8$N$_2$Na$_2$O$_2$Ru$_2$S$_4$ (M): m/z 961.64. Found: m/z 901.93 [M + H$^+$; DMSO + H$_2$O], 943.86 [M − Cl + H$_2$O], 962.02 [M + H$^+$]. IR (Figure S8; ν_{max}, cm^{-1}): 3500−3000 (s) [C−H], 1705 (s), 1610 (m) [C=N], 1422 (s), 1363 (m), 1222 (m) [CH$_2$], 1089 (m), 1022 (m) [(S=O)(DMSO)], 815 (s) [C−S], 530 (m) [S−S].

The detailed synthetic procedure adopted for the preparation of RuPySSPyRu is described in the Supporting Information.

HEWL Crystallization. HEWL crystals were grown by hanging-drop vapor diffusion,[36] mixing 1 μL of 15 mg mL^{-1} protein in sodium acetate at pH 4.5 with 1 μL of 1.1 M sodium chloride and 50 mM sodium acetate at pH 4.5. Very well-shaped crystals had rapidly grown within 48 h and were soaked by merging a 2 μL drop of a 15 mM

AziRu aqueous solution to the 2 μL crystal drop. The solution suddenly turned yellowish and so did the crystals upon AziRu exposure, thus turning to a greenish color in a time scale of hours and eventually becoming dark brown/black in 1 week, as previously reported.[25,26] Crystals were kept at 20 °C throughout the whole crystallization, soaking, and color shift process. Black crystals were exposed to the alternative reduction with sodium borohydride, hydrazine, and sodium ascorbate. Different reducing agent concentrations were tested (i.e., 10, 20, 50, and 100 mM reductant concentration in 50 mM sodium acetate at pH 4.5) corresponding to 1, 2, 5, and 10 molar ratio, respectively, with respect to the Ru^{III} concentration used for soaking, but no significant differences were evidenced.

Raman Microspectroscopy. Raman data were collected at increasing time from soaking until the formation of black crystals by using a commercial Jasco NSR-3100 spectrometer and a 514 nm excitation laser line (3 mW at sample power, 20× lens, 7 cm^{-1} spectral resolution) directly in the crystallization well. Further details are provided elsewhere.[37]

X-ray Crystallography. The best-looking black crystals were chosen for X-ray data collection, which was performed using a Saturn 944 charge-coupled detector along with Cu Kα X-ray radiation from a Rigaku Micromax 007 HF generator, and processed using HKL2000.[38] The very same black crystal used for the reference data set collection was subjected to reduction and subsequently reused for X-ray data collection. The phasing was carried out by molecular replacement using *Phaser* software[39] and the 4J1B[25] model from the PDB as a template. Crystallographic refinements were performed using *Coot 0.8.6*[40] and *REFMAC5* from the *CCP4* software suite.[41]

SERS. SERS measurements were carried out with the AziRu disulfide derivative (RuPySSPyRu) to establish a self-assembled monolayer on a Au electrode surface, which allowed potential-controlled experiments (Figures 4−6). The electrode preparation started with mechanical cleaning by using abrasive fine dust and sandpaper with progressively narrowing texture, followed by treatment with a 1:1 (v/v) H_2O_2/H_2SO_4 solution and finally an ultrasonic bath for 15 min. Subsequently, the Au surface was roughened through an electrochemical process by using 0.1 M potassium chloride as the electrolyte solution and redox cycles under a protective argon atmosphere. RuPySSPyRu that formed a self-assembled monolayer (RuPyS-SAM) was obtained by dipping the roughened electrode into a 1:1 H_2O/ethanol/15 mM RuPySSPyRu solution overnight, with the cell carefully sealed. The functionalized Au ring electrodes were mounted on a spinning shaft in a 10 mL electrochemical cell. During the measurements, the electrode was kept spinning at 200 Hz to reduce laser-induced photochemical reactions of RuPyS-SAM. The Au ring itself served as the working electrode, while Ag/AgCl and Pt wires were used as reference and counter electrode, respectively. The conducting rotating shaft, carrying the Au ring electrode, was connected to a speed-controlled motor and a potentiostat. SERS spectra were collected by using a LabRAM HR800 system equipped with an Olympus BX41 microscope (20× objective from Nikon) and a 647 nm Coherent Innova Kr$^+$ laser line. A Peltier-cooled Andor charge-coupled detector operating at −70 °C and a 180°-oriented notch filter completed the setup. All reported spectra were recorded at room temperature, a laser power of 1 mW at the sample, and a spectral resolution of 1 cm^{-1}. All of the buffers used in this work included 10 mM $Na_2B_4O_7$/NaOH, 100 mM KCl at pH 10, 10 mM Na_2HPO_4/NaH_2PO_4, 100 mM KCl at pH 7, 10 mM sodium acetate, and 100 mM KCl at pH 4, and the pH was accordingly adjusted for intermediate values.

■ RESULTS AND DISCUSSION

Ru Chemical Reduction and Release from a Model Protein. Upon exposure to the AziRu solution, the lysozyme native crystals swiftly turned yellowish (in minutes), then greenish (in hours), and later black (≥1 week), consistent with previous results.[25,26] Black crystals remained stable for 1 year.

The Raman spectra from the native and black crystals were collected as starting references for the reduction/release process (Figure 2). The black crystal trace shows very strong
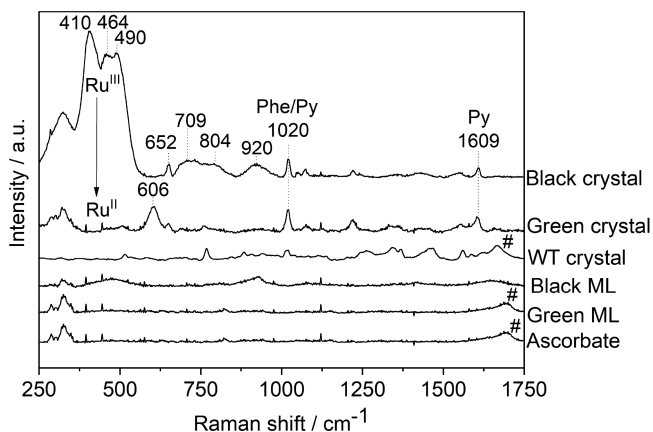

Figure 2. Nonresonant Raman spectra of the reduction of the lysozyme AziRu^{III} (black crystals) and lysozyme AziRu^{II} (green crystals) upon ascorbate exposure. The wild-type lysozyme crystal spectrum is also reported as a reference, as well as the ML from either green or black crystals. Spectral features marked by asterisks refer to signals from the ML, whereas those labeled by "#" refer to signals from ascorbate.

Raman bands in the low-frequency region arising from the Ru^{III}-OH_2/OH^- (400−500 cm^{-1}) and Ru^{IV}-O-Ru^{IV} (500−700 cm^{-1}) according to previous assignments.[25,26] Possible Ru^{III}-Cl^- modes are located below ca. 300 cm^{-1}.[42] Conversely, spectral contributions from the mother liquor (ML) and protein are negligible.

The crystallographic structure of the black crystal was solved (Table S1 and Figure 3A), and as expected, the model closely resembles the previously solved structure (PDB accession 4J1B).[25] The Ru binding site is at the His15 side chain (Ru-NE2 at 2.4 Å), and its occupancy was evaluated to be 0.5, in contrast to that found in the case of NAMI-A, which binds Asp side chains.[43] The Ru bound to His15 exhibits octahedral geometry, although the sixth ligand (wat in Figure 3A,C) could not be interpreted as part of the Ru coordination sphere because of significant geometrical distortion. This can be due to the steric hindrance by the close-by Asp87 side chain that competes for ligation.

Chemical reduction was performed on black crystals using three different reducing agents (sodium borohydride, hydrazine, and sodium ascorbate). The exposure to borohydride rapidly destroyed the crystal due to vigorous hydrogen evolution so that neither Raman nor crystallographic investigations were possible. By contrast, hydrazine (chosen as a well-known reductant and ligand of Ru) led to a colorless, native-like crystal, whose Raman spectrum (data not shown) is indistinguishable from that of native lysozyme crystals grown under the same conditions. This finding clearly indicates that Ru^{III} reduction itself is not sufficient to induce Ru^{II} release (see below), possibly requiring two events along the reduction−release mechanism,[44] as in

Ru^{III}(aquated)-HEWL

$\rightarrow Ru^{II}$(aquated)-HEWL

$\rightarrow Ru^{II}$(aquated)+HEWL
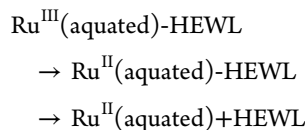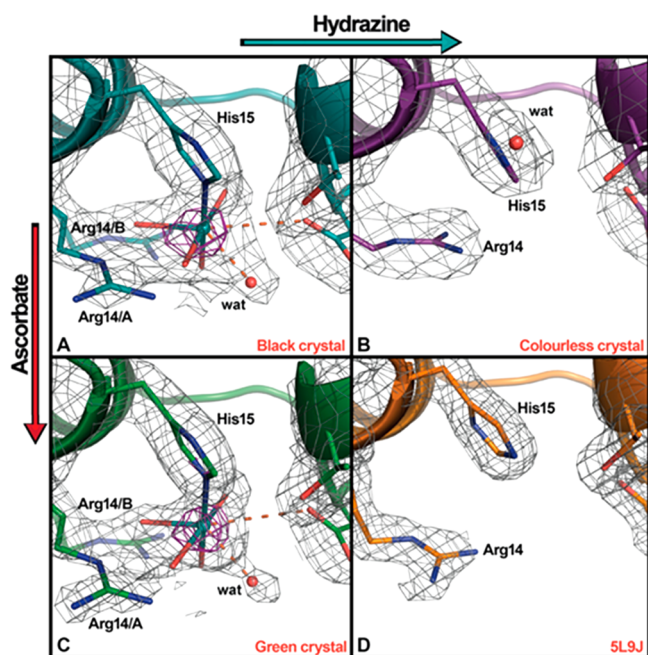
Figure 3. Closeup of the crystallographic models for the His15 Ru binding site. All models are countered with $2F_o - F_c$ at 1σ (gray mesh) and 3σ (purple mesh). For the sake of clarity, noninteracting H_2O molecules were hidden. (A) Detail for the black crystal before chemical reduction. (B) Upon reduction with hydrazine, no Ru density is detectable. (C) Upon reduction with ascorbate, no significant structural modification is noted, and the Ru density is almost unperturbed. (D) Native lysozyme structure from crystals grown in the same conditions is reported as a reference (PDB 5L9J).

Indeed, upon hydrazine addition, the X-ray structure (solved at 2.55 Å and refined at R and R_{free} values of 0.193 and 0.293, respectively; Table S1) did not show any residual Ru density (Figure 3B) and resembled the wild-type lysozyme structure of crystals grown under the same conditions (Figure 3D; PDB 5L9J), as also confirmed by the low 0.279 Å root-mean-square deviation (RMSD) calculated by superimposing the hydrazine-reduced model to PDB 5L9J.[45]

By contrast, the black crystal turned back to green upon reduction with ascorbate and remained in this state long enough to allow for Raman and X-ray diffraction data collection. The Raman spectrum distinctly changed by completely losing the very strong Ru^{III}-H_2O/OH^- signals in the low-frequency region (from a black to green crystal trace in Figure 2), suggesting that $Ru^{III} \rightarrow Ru^{II}$ reduction occurred, with no Ru release. Instead, a new band at around 606 cm^{-1} was observed in the spectrum of the green crystal, which may originate from the Ru^{II}-Cl^- stretching, as reported previously for the mixed-valence $[Ru^{II/III}_2(NH_3)_6Cl_3]^{2+}$ complex.[46] An alternative assignment to the ML, ascorbate, or protein can safely by ruled by a comparison with the corresponding Raman spectra (Figure 2).

The crystallographic structure for the ascorbate-reduced crystal (green crystal) was solved at 1.86 Å and refined up to R and R_{free} values of 0.178 and 0.255, respectively (Table S1). Unlike reduction with hydrazine, this crystal revealed the persistence of Ru bound to His15 with almost no difference compared to the black crystal structure (Figure 3C). Electron-density maps indicated that no disulfide reduction occurred and the Ru site kept its occupancy and coordination geometry. The RMSD value obtained by superimposing the structures of

the green and black crystals is as low as 0.125 Å, indicating that the structures are almost identical.

The ascorbate-reduced complex lacking the characteristic Ru^{III}-H_2O/OH^- Raman bands showed Ru density in the reduced crystal structure, indicating a Ru^{II} species bound to the protein:

$$Ru^{III}(\text{aquated})\text{-HEWL} \rightarrow Ru^{II}(\text{aquated})\text{-HEWL}$$
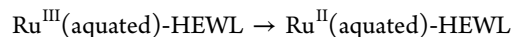
In this case, Ru^{II} was still bound to the protein, in contrast to that observed by reduction with hydrazine. This difference may originate from (i) the different redox potentials (ca. −115 and −435 mV, respectively, vs 3 M KCl/Ag/AgCl)[47,48] and/or (ii) different operative mechanisms. Because no redox-active amino acid that could be involved in the redox process was in proximity to the Ru complex, we favor the latter option. It could be that, in the case of hydrazine, the presence of potential N-coordinating ligands may promote the Ru^{II} release.

The aggregate of inference from diverse hydrazine- and ascorbate-induced action is supportive of a two-step Ru reduction−release mechanism (as described above for hydrazine).

AziRu pK_a and E_0 as a Function of the pH. The mechanism of action of AziRu involves a complex process dependent on the pH, redox potential, and binding to proteins or nucleic acids. To isolate the pH and redox-potential dependence according to the simplified model shown in Scheme 1, which involves a redox transition in each the

Scheme 1. Simplified Model for the pH and Redox Dependence of Hydrated AziRu Complexes Involving a Minimal Amount of Subsequent (De)protonation and Redox Steps (with X = H_2O or Cl^-)[a]
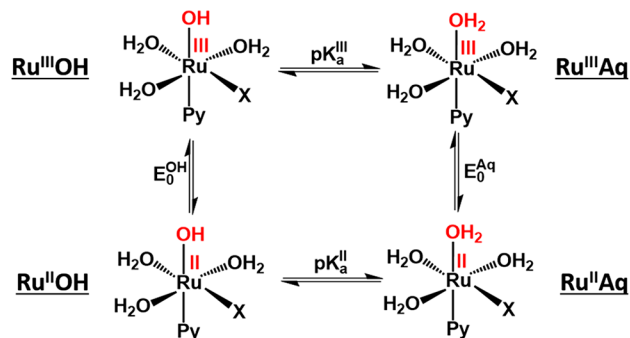
[a]The Ru redox state and (de)protonable H_2O/OH^- ligand are highlighted in red. Potential ligand-exchange processes are not considered in this scheme.

protonated and deprotonated states of the complex, we performed SERS experiments using an AziRu derivative (named RuPySSPyRu, where Py stands for pyridine) designed as a surrogate and simple model for Ru^{III} complexes that can undergo reduction. This new Ru^{III}-based complex was specifically prepared for these experiments because its disulfide allowed immobilization onto the Au surface, also forming a self-assembled monolayer (SAM) on Au electrodes (see the Supporting Information for synthesis and characterization details).

RuPyS-SAM (Figure 4) allowed monitoring of the potential- and pH-dependent processes by SERS experiments, performed in comparison with the nonruthenated 4-pyridineethanethiol SAM (PyS-SAM). As shown in Figure 4 (top) and according
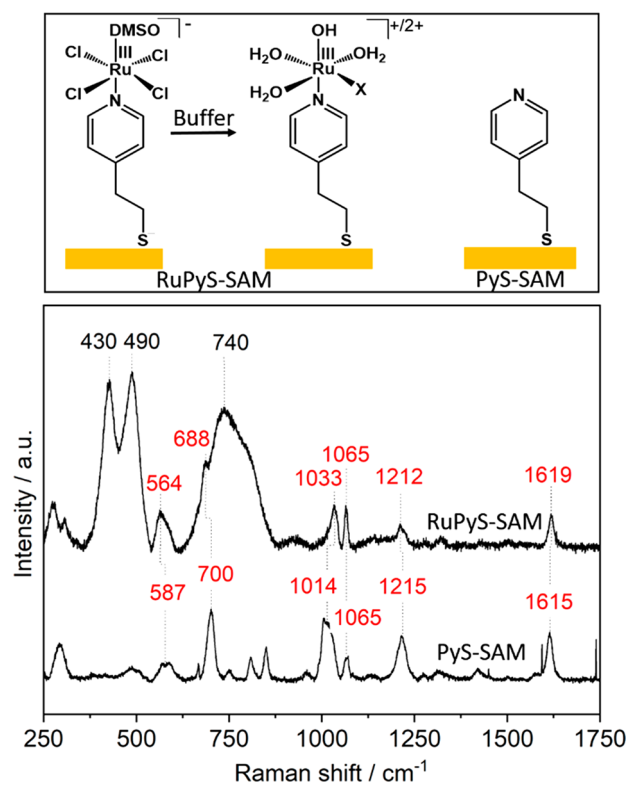
Figure 4. (Top) Schematic representation of the RuPyS-SAMs and PyS-SAMs on Au electrodes used in this work. Upon immersion of RuPyS-SAM into an aqueous buffer, ligand exchange takes place with X = H$_2$O or Cl$^-$. (Bottom) SERS spectra (647 nm) of RuPyS-SAM and PyS-SAM in the buffer at pH 7. Red and black labels refer to peaks assigned to PyS-SAM and Ru-ligand modes, respectively.

to Webb and Walsby's work,[49] the chloride and DMSO ligands are exchanged with bulk H$_2$O so that the prevailing species in the SERS spectra are [Ru^{III}(Py)Cl(H$_2$O)$_3$OH]$^+$ or [Ru^{III}(Py)(H$_2$O)$_4$OH]$^{2+}$ if no redox transition takes place. A comparison with the SERS spectrum of 4-pyridineethanethiol SAM (PyS-SAM; see the scheme in Figure 4, top) reveals that the SERS spectrum of the aquated RuPyS-SAM in the region above 1000

cm^{-1} is dominated by bands of the pyridyl moiety, which were assigned previously.[50] In the low-frequency region (<1000 cm^{-1}), however, only the peaks at 688 and 564 cm^{-1} can be directly assigned to the modes of PyS-SAM. Similar to the protein-associated species in Figure 2, the peaks at 430 and 490 cm^{-1} and the broad features at 740 cm^{-1} can be ascribed to Ru^{III}-OH$_2$/OH$^-$ and to coordinated H$_2$O-ligand modes, respectively, in agreement with theoretical calculations (see the Supporting Information).

In order to study the pH-dependent behavior of the AziRu disulfide analogue, we performed a pH titration of RuPyS-SAM in the pH 4−10 range (Figure 5, right) by exchanging the supernatant solution covering the SAM. In particular, in the low-frequency range, the modes associated with the H$_2$O/OH$^-$ ligands change considerably in position and relative intensity. On the basis of the assumptions that no significant pH-induced redox transition occurs (as is deduced from a comparison with potential-dependent data in Figure 6), that only two species contribute to the spectra, i.e., the oxidized basic and acidic ones (referred to as "Ru^{III}OH" and "Ru^{III}Aq", respectively; see Scheme 1), and that the spectrum at pH 10 consists purely of "Ru^{III}OH", we performed a global fit over the entire pH range. Plotting the fraction of the "Ru^{III}OH" component spectrum contributing to the overall spectra against the pH shows sigmoidal behavior with an apparent pK_a^{III} value of 6.0 ± 0.4. The relatively broad transition was not unexpected because the pK_a value of a single Ru complex depends on the protonation state of the neighboring Ru sites. Furthermore, the transition may involve not only the protonation of OH$^-$ ligands but also the concomitant H$_2$O/Cl$^-$ ligand exchange that may occur in several steps. Nevertheless, the pK_a value determined from this curve may be considered as a good estimation of single AziRu entities. Interestingly, this pK_a value lies in range close to pH values typical of cancer lumen, indicating that changes in the pH can indeed efficiently affect the protonation pattern of Ru^{III} ligands.

In order to examine the electrochemical behavior, we performed redox titrations at pH 10 and 4, where the deprotonated "Ru^{III}OH" and protonated "Ru^{III}Aq" species prevail at oxidizing electrode potentials, respectively, according to the apparent pK_a^{III} determined above (Figure 6 and Scheme
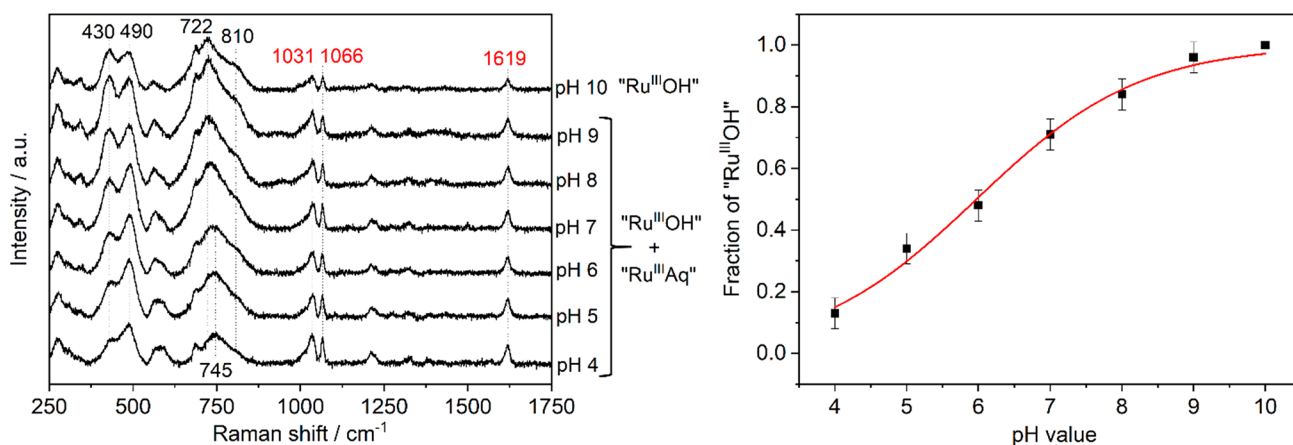
Figure 5. (Left) SERS spectroscopic pH titration (647 nm) of RuPyS-SAM in aqueous buffers. As described in the main text, the spectrum at pH 10 was assumed to represent a pure deprotonated "Ru^{III}OH" species, while the other spectra were attributed to a mixture of deprotonated "Ru^{III}OH" and protonated "Ru^{III}Aq" species. Red and black labels refer to peaks assigned to the PyS-SAM and Ru ligand modes, respectively. (Right) Plot of the fraction of the "Ru^{III}OH" component in the SERS pH titration against the pH value. The fit of a sigmoidal curve, $y = y_2 + (y_1 - y_2)/\{1 + \exp[(\text{pH} - pK_a)/c]\}$, to the data yielded the following results: $y_2 = 1.00$; $y_1 = 0.03 \pm 0.15$; $pK_a = 6.0 \pm 0.4$; $c = 1.1 \pm 0.3$.
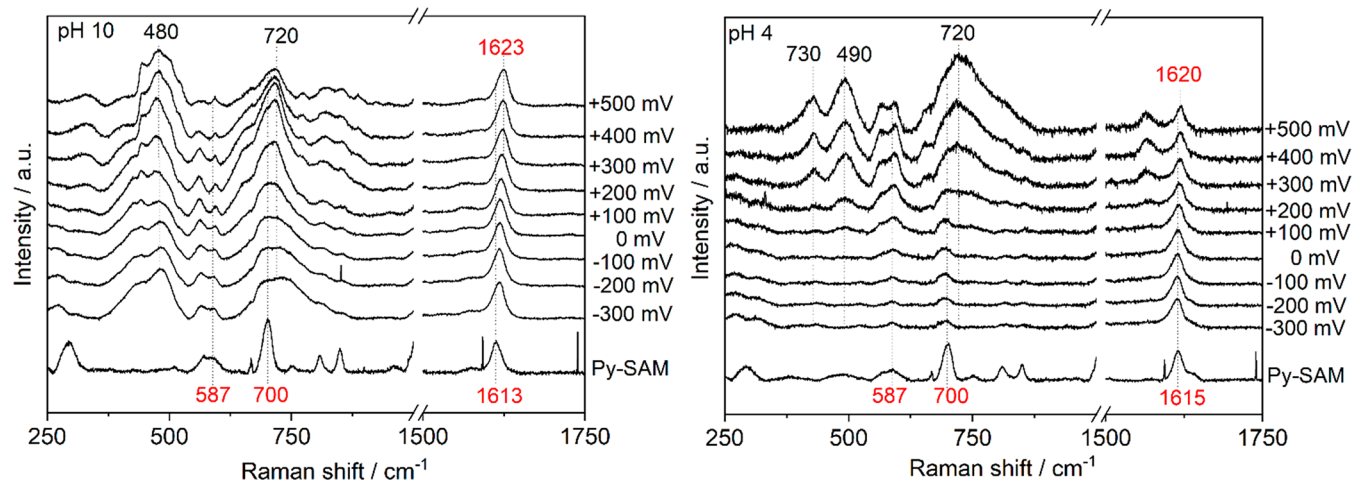
Figure 6. SERS spectroscopic redox titrations (647 nm) of RuPyS-SAM in aqueous buffers at pH 10 (left) and pH 4 (right). Red and black labels refer to peaks assigned to the PyS-SAM and Ru ligand modes, respectively. The fit of the Nernst equation to the data at pH 4 is shown in the Supporting Information.

1). Understanding the potential-dependent changes of the SERS spectra is not straightforward because changes, e.g., of ligation and/or the vibrational Stark effect,[51] can superimpose redox transitions of the Ru complex. However, it is striking that the spectral pattern of the Ru-OH$_2$/OH$^-$ modes at 430, 490, and 720 cm^{-1} disappears upon lowering the potential below +100 mV only at pH 4, while at pH 10, these modes persist over the entire potential range and only changes in the relative intensity and position were observed. Furthermore, the spectra in the <−100 mV potential range at pH 4 exhibited peaks at, e.g., 587, 700, and 1615 cm^{-1}, with exactly the same positions as those for PyS-SAM. The absence of bands of the Ru^{II} species at pH 4 may be interpreted in terms of a substantially lowered Raman cross section compared to the Ru^{III} species at pH 4 and 10, due to different ligation patterns and redox states, as reflected by the different redox potentials at pH 4 and 10 (see below). Interestingly, this behavior at pH 4 resembles the spectral changes from black to green crystals upon treatment with ascorbate at pH 4.5, i.e., the disappearance of the peaks at 400−500 and 680−820 cm^{-1} (Figure 2), and therefore supports the interpretation of a successful reduction under these conditions. Furthermore, this supports the previous assumption that no significant redox transition occurred in Figure 5 and thus validates the pK_a^{III} determined above. Employing the same approach as that for the determination of pK_a, we can estimate the redox potentials at both pH values to be E_0(pH 4) ≈ +300 mV and E_0(pH 10) < −300 mV (see the Supporting Information). The former value can contain a considerable error because the spectral changes did not reach a plateau at oxidative potentials. However, considering Scheme 1 as the simplest model of the proton-coupled redox changes of RuPyS-SAM, we can provide an estimation for the pK_a^{II} in the reduced state using the Nernst and Hasselbach−Henderson equations for each transition. Accordingly, assuming similarly broad transitions in both pH and redox transitions, the pK_a and E_0 values are related by

$$c_E^{-1}(E_0^{Aq} - E_0^{OH}) = c_{pH}^{-1}(pK_a^{II} - pK_a^{III}) \qquad (1)$$

where c_E and c_{pH} are the constants determined from the sigmoidal plots in Figures S11 and 5 and yield a pK_a^{II} > 14.7. This estimation is in line with Ru^{II}Aq being the prevailing reduced state in the range of physiological pH values.

Furthermore, it shows that the protonation of ligands indeed facilitates the reduction of the Ru center.

Because, to the best of our knowledge, none of these values was reported previously for aquated AziRu derivatives, it is now interesting to compare these redox potentials to those determined using the formalism of Lever (Table S2).[52] The Lever equation is an empirical model that considers the contribution of ligands to the redox potential of metal ions in an additive fashion and was calibrated previously for many metals in different redox states and a plethora of common ligands. Accordingly, for the redox couples Ru$^{II/III}$Py(H$_2$O)$_5$ and Ru$^{II/III}$PyCl(H$_2$O)$_4$, which may correspond to redox-active species of RuPyS-SAM, the redox potentials of −70 and −180 mV were predicted. The mismatch of these values and the values determined in this work may be rationalized in terms of electrostatic interactions between the individual AziRu analogue units within the SAM and the coupling of electron transfer, protonation steps, and ligand-exchange reactions. However, in both cases, the redox potentials lie in a range in which biological reducing agents could facilitate a redox transition. Furthermore, according to Lever's formalism, for the deprotonated counterparts, the redox potentials are shifted by ca. −530 and −460 mV, respectively, which matches the experimentally estimated shift of ca. −600 mV. We expect that the nature of the ligands (e.g., pyridine in lieu of imidazole, which is the main structural difference between AziRu and NAMI-A) will modulate pK_a and E_0, but the underlying mechanism may follow this scheme for Ru^{III} complexes in general and therefore also for the pH-facilitated redox transition of the imidazole-ligated Ru^{III}-HEWL complex as demonstrated above.

■ CONCLUSIONS

AziRu represents a very promising prodrug from the Ru-based complex family because of its antimetastatic and likely selectivity properties.[20,22] The keystone hypothesis underlying the selective activation of the prodrug harks back to whether the reduction of the Ru complex within cancerous lesions could occur more easily than in the physiological counterparts because of two checkpoints: the lower pH in the cancer extracellular lumen and the sensibly higher reducing potential of cancerous cytosol. In fact, the pH sensitivity of Ru^{III}

reduction could be demonstrated by potential-dependent SERS, revealing a pK_a value of 6.0 ± 0.4 for the immobilized and hydrated AziRu model compound associated with a protonation-dependent shift of the redox potential by at least 600 mV.

The Raman-assisted crystallography provided clues on the mechanism of Ru release from protein upon reduction. Indeed, the outcome evidently depended on the reducing agent. Reduction with hydrazine produced a native-like lysozyme crystal because no trace of the residual Ru electron density was found and the Raman spectrum was identical with the native one, convincingly supportive of the Ru^{II} release from the protein. By contrast, reduction by ascorbate yielded the AziRu-soaked black crystal (Ru^{II}/Ru^{III}) firmly back to green (Ru^{II}) without Ru release. Altogether, the diverse hydrazine- and ascorbate-induced action is supportive of a two-step Ru reduction−release mechanism.

■ ASSOCIATED CONTENT

Ⓢ Supporting Information

The Supporting Information is available free of charge on the ACS Publications website at DOI: 10.1021/acs.inorgchem.8b02667.

Synthesis and characterization, ^{1}H and ^{13}C NMR, MALDI-TOF, ESI-MS, overlapped UV−vis, and IR spectra, density functional theory (DFT) assignment of the Raman spectra, Nernst fit to redox titration, plot of the fraction of the "Ru^{III}Aq" component, Tables S1 and S2, and optimized geometries of DFT calculations (PDF)

■ AUTHOR INFORMATION

Corresponding Authors
*E-mail: avergara@unina.it (A.V.).
*E-mail: jkozuch@stanford.edu (J.K.).

ORCID Ⓞ
Antonello Merlino: 0000-0002-1045-7720
Daniela Montesarchio: 0000-0001-6295-6911
Maria A. Mroginski: 0000-0002-7497-5631
Alessandro Vergara: 0000-0003-4135-0245

Present Address
⊥Department of Chemistry, Stanford University, Stanford, CA 94305-5012.

Author Contributions
§These authors contributed equally. A.V., J.K., P.H., and L.P. conceived the research project. M.C., M.H., F.R., J.K., and A.V. performed the experiments. J.K. and M.A.M. performed DFT calculations. M.C. and A.M. carried out X-ray crystallography. D.Mo., D.Mu., and C.R. conducted organic synthesis. The manuscript was written through contributions of all authors. All authors have given approval to the final version of the manuscript.

Notes
The authors declare no competing financial interest.

■ REFERENCES

(1) Cardone, R.; Casavola, V.; Reshkin, S. The role of disturbed pH dynamics and the Na+/H+ exchanger in metastasis. *Nat. Rev. Cancer* **2005**, *5* (10), 786−795.

(2) Wardman, P. Electron transfer and oxidative stress as key factors in the design of drugs selectively active in hypoxia. *Curr. Med. Chem.* **2001**, *8* (7), 739−61.

(3) Merlino, A. Interactions between proteins and Ru compounds of medicinal interest: A structural perspective. *Coord. Chem. Rev.* **2016**, *326*, 111−134.

(4) Schluga, P.; Hartinger, C. G.; Egger, A.; Reisner, E.; Galanski, M.; Jakupec, M. A.; Keppler, B. K. Redox behavior of tumor-inhibiting ruthenium(III) complexes and effects of physiological reductants on their binding to GMP. *Dalton T* **2006**, No. 14, 1796−1802.

(5) Levina, A.; Mitra, A.; Lay, P. A. Recent developments in ruthenium anticancer drugs. *Metallomics* **2009**, *1* (6), 458−70.

(6) Reisner, E.; Arion, V. B.; Keppler, B. K.; Pombeiro, A. J. L. Electron-transfer activated metal-based anticancer drugs. *Inorg. Chim. Acta* **2008**, *361* (6), 1569−1583.

(7) Dragutan, I.; Dragutan, V.; Demonceau, A. Editorial of Special Issue Ruthenium Complex: The Expanding Chemistry of the Ruthenium Complexes. *Molecules* **2015**, *20* (9), 17244−17274.

(8) Graf, N.; Lippard, S. J. Redox activation of metal-based prodrugs as a strategy for drug delivery. *Adv. Drug Delivery Rev.* **2012**, *64* (11), 993−1004.

(9) Clarke, M. J. Toward ruthenium containing metallopharmaceuticals. *Abstr Pap Am. Chem. S* **2005**, *230*, U2131−U2131.

(10) Jakupec, M. A.; Reisner, E.; Eichinger, A.; Pongratz, M.; Arion, V. B.; Galanski, M.; Hartinger, C. G.; Keppler, B. K. Redox-active antineoplastic ruthenium complexes with indazole: correlation of in vitro potency and reduction potential. *J. Med. Chem.* **2005**, *48* (8), 2831−7.

(11) Alessio, E.; Messori, L. In *Metallo-Drugs: Development and Action of Anticancer Agents*; Berlin, 2018; Chapter 5, pp 141−170.

(12) Gianferrara, T.; Bratsos, I.; Alessio, E. A categorization of metal anticancer compounds based on their mode of action. *Dalton Trans.* **2009**, *37*, 7588−7598.

(13) Han Ang, W.; Dyson, P. J. Classical and non-classical ruthenium-based anticancer drugs: Towards targeted chemotherapy. *Eur. J. Inorg. Chem.* **2006**, *2006*, 4003−4018.

(14) Markowska, A.; Kasprzak, B.; Jaszczynska-Nowinka, K.; Lubin, J.; Markowska, J. Noble metals in oncology. *Wspolczesna Onkol.* **2015**, *4*, 271−275.

(15) Antonarakis, E. S.; Emadi, A. Ruthenium-based chemotherapeutics: are they ready for prime time? *Cancer Chemother. Pharmacol.* **2010**, *66* (1), 1−9.

(16) Leijen, S.; Burgers, S. A.; Baas, P.; Pluim, D.; Tibben, M.; van Werkhoven, E.; Alessio, E.; Sava, G.; Beijnen, J. H.; Schellens, J. H. M. Phase I/II study with ruthenium compound NAMI-A and gemcitabine in patients with non-small cell lung cancer after first line therapy. *Invest. New Drugs* **2015**, *33* (1), 201−214.

(17) Meier-Menches, S. M.; Gerner, C.; Berger, W.; Hartinger, C. G.; Keppler, B. K. Structure-activity relationships for ruthenium and osmium anticancer agents - towards clinical development. *Chem. Soc. Rev.* **2018**, *47* (3), 909−928.

(18) Sava, G.; Pacor, S.; Bergamo, A.; Cocchietto, M.; Mestroni, G.; Alessio, E. Effects of Ruthenium Complexes on Experimental-Tumors - Irrelevance of Cytotoxicity for Metastasis Inhibition. *Chem.-Biol. Interact.* **1995**, *95* (1−2), 109−126.

(19) Webb, M. I.; Chard, R. A.; Al-Jobory, Y. M.; Jones, M. R.; Wong, E. W. Y.; Walsby, C. J. Pyridine Analogues of the Antimetastatic Ru(III) Complex NAMI-A Targeting Non-Covalent Interactions with Albumin. *Inorg. Chem.* **2012**, *51* (2), 954−966.

(20) Simeone, L.; Mangiapia, G.; Vitiello, G.; Irace, C.; Colonna, A.; Ortona, O.; Montesarchio, D.; Paduano, L. Cholesterol-based nucleolipid-ruthenium complex stabilized by lipid aggregates for antineoplastic therapy. *Bioconjugate Chem.* **2012**, *23* (4), 758−70.

(21) Musumeci, D.; Rozza, L.; Merlino, A.; Paduano, L.; Marzo, T.; Massai, L.; Messori, L.; Montesarchio, D. Interaction of anticancer

Ru(III) complexes with single stranded and duplex DNA model systems. *Dalton T* **2015**, *44* (31), 13914−13925.

(22) Mangiapia, G.; D'Errico, G.; Simeone, L.; Irace, C.; Radulescu, A.; Di Pascale, A.; Colonna, A.; Montesarchio, D.; Paduano, L. Ruthenium-based complex nanocarriers for cancer therapy. *Biomaterials* **2012**, *33* (14), 3770−82.

(23) Riccardi, C.; Musumeci, D.; Irace, C.; Paduano, L.; Montesarchio, D. Ru-III Complexes for Anticancer Therapy: The Importance of Being Nucleolipidic. *Eur. J. Org. Chem.* **2017**, *2017*, 1100−1119.

(24) Acampora, F.; Marzaioli, A. M.; Capuozzo, A.; Appavou, M. S.; Campanella, A.; D'Errico, G.; Irace, C.; Montesarchio, D.; Musumeci, D.; Szekely, N. K.; Santamaria, R.; De Castro, C.; Paduano, L. Lipooligosaccharides as Amphiphiles to Build Liposomes for Effective Drug Delivery: The Case of Anticancer Ruthenium Complex-Based Aggregates. *Chemistryselect* **2016**, *1* (10), 2129−2139.

(25) Vergara, A.; D'Errico, G.; Montesarchio, D.; Mangiapia, G.; Paduano, L.; Merlino, A. Interaction of Anticancer Ruthenium Compounds with Proteins: High-Resolution X-ray Structures and Raman Microscopy Studies of the Adduct between Hen Egg White Lysozyme and AziRu. *Inorg. Chem.* **2013**, *52* (8), 4157−4159.

(26) Vergara, A.; Russo Krauss, I.; Montesarchio, D.; Paduano, L.; Merlino, A. Investigating the ruthenium metalation of proteins: X-ray structure and Raman microspectroscopy of the complex between RNase A and AziRu. *Inorg. Chem.* **2013**, *52* (19), 10714−6.

(27) Vergara, A.; Vitagliano, L.; Verde, C.; di Prisco, G.; Mazzarella, L. Spectroscopic and crystallographic characterization of bis-histidyl adducts in tetrameric hemoglobins. *Methods Enzymol.* **2008**, *436*, 425−444.

(28) Vergara, A.; Vitagliano, L.; Merlino, A.; Sica, F.; Marino, K.; Verde, C.; di Prisco, G.; Mazzarella, L. An Order-Disorder Transition Plays a Role in Switching Off the Root Effect in Fish Hemoglobins. *J. Biol. Chem.* **2010**, *285* (42), 32568−32575.

(29) Merlino, A.; Verde, C.; di Prisco, G.; Mazzarella, L.; Vergara, A. Reduction of ferric hemoglobin from Trematomus bernacchii in a partial bis-histidyl state produces a deoxy coordination even when encapsulated into the crystal phase. *Spectroscopy* **2008**, *22* (2−3), 143−152.

(30) Di Fiore, A.; Vergara, A.; Caterino, M.; Alterio, V.; Monti, S. M.; Ombouma, J.; Dumy, P.; Vullo, D.; Supuran, C. T.; Winum, J. Y.; De Simone, G. Hydroxylamine-O-sulfonamide is a versatile lead compound for the development of carbonic anhydrase inhibitors. *Chem. Commun.* **2015**, *51* (57), 11519−11522.

(31) Caterino, M.; Petruk, A. A.; Vergara, A.; Ferraro, G.; Marasco, D.; Doctorovich, F.; Estrin, D. A.; Merlino, A. Mapping the protein-binding sites for iridium(III)-based CO-releasing molecules. *Dalton T* **2016**, *45* (30), 12206−12214.

(32) Petruk, A. A.; Vergara, A.; Marasco, D.; Bikiel, D.; Doctorovich, F.; Estrin, D. A.; Merlino, A. Interaction between Proteins and Ir Based CO Releasing Molecules: Mechanism of Adduct Formation and CO Release. *Inorg. Chem.* **2014**, *53* (19), 10456−10462.

(33) Caterino, M.; Merlino, A.; Balsamo, A.; Russo Krauss, I.; Parisi, S.; Vergara, A. Reaction of Hg2+ Insertion into Cysteine Pairs Within Bovine Insulin Crystals Followed via Raman Spectroscopy. *J. Solution Chem.* **2014**, *43* (1), 135−143.

(34) Murgida, D. H.; Hildebrandt, P. Electron-transfer processes of cytochrome c at interfaces. New insights by surface-enhanced resonance Raman spectroscopy. *Acc. Chem. Res.* **2004**, *37* (11), 854−861.

(35) Alessio, E.; Balducci, G.; Calligaris, M.; Costa, G.; Attia, W. M.; Mestroni, G. Synthesis, Molecular-Structure, and Chemical Behavior of Hydrogen Trans-Bis(Dimethyl Sulfoxide)Tetrachlororuthenate(Iii) and Mer-Trichlorotris(Dimethyl Sulfoxide)Ruthenium(Iii) - the 1st Fully Characterized Chloride Dimethyl-Sulfoxide Ruthenium(Iii) Complexes. *Inorg. Chem.* **1991**, *30* (4), 609−618.

(36) Vergara, A.; Lorber, B.; Sauter, C.; Giegé, R.; Zagari, A. Lessons from crystals grown in the Advanced Protein Crystallisation Facility for conventional crystallisation applied to structural biology. *Biophys. Chem.* **2005**, *118* (2−3), 102−112.

(37) Vergara, A.; Merlino, A.; Pizzo, E.; D'Alessio, G.; Mazzarella, L. A novel method for detection of selenomethionine incorporation in protein crystals via Raman microscopy. *Acta Crystallogr., Sect. D: Biol. Crystallogr.* **2008**, *64*, 167−171.

(38) Otwinowski, Z.; Minor, W. Processing of X-ray diffraction data collected in oscillation mode. *Methods Enzymol.* **1997**, *276*, 307−26.

(39) McCoy, A. J.; Grosse-Kunstleve, R. W.; Adams, P. D.; Winn, M. D.; Storoni, L. C.; Read, R. J. Phaser crystallographic software. *J. Appl. Crystallogr.* **2007**, *40* (4), 658−674.

(40) Emsley, P.; Lohkamp, B.; Scott, W. G.; Cowtan, K. Features and development of Coot. *Acta Crystallogr., Sect. D: Biol. Crystallogr.* **2010**, *66* (4), 486−501.

(41) Murshudov, G. N.; Skubak, P.; Lebedev, A. A.; Pannu, N. S.; Steiner, R. A.; Nicholls, R. A.; Winn, M. D.; Long, F.; Vagin, A. A. REFMAC5 for the refinement of macromolecular crystal structures. *Acta Crystallogr., Sect. D: Biol. Crystallogr.* **2011**, *67* (4), 355−367.

(42) Durig, J. R.; Omura, Y.; Mercer, E. E. Far infrared and raman spectra and structure of ruthenium halogenoammine complexes. *J. Mol. Struct.* **1975**, *29* (1), 53−63.

(43) Messori, L.; Merlino, A. Ruthenium metalation of proteins: the X-ray structure of the complex formed between NAMI-A and hen egg white lysozyme. *Dalton T* **2014**, *43* (16), 6128−6131.

(44) Santos, R. L. S. R.; van Eldik, R.; de Oliveira Silva, D. Kinetic and mechanistic studies on reactions of diruthenium(II,III) with biologically relevant reducing agents. *Dalton T* **2013**, *42* (48), 16796−16805.

(45) Crosas, E.; Castellvi, A.; Crespo, I.; Fulla, D.; Gil-Ortiz, F.; Fuertes, G.; Kamma-Lorger, C. S.; Malfois, M.; Aranda, M. A. G.; Juanhuix, J. Uridine as a new scavenger for synchrotron-based structural biology techniques. *J. Synchrotron Radiat.* **2017**, *24*, 53−62.

(46) Armstrong, R. S.; Horsfield, W. A.; Nugent, K. W. Assignment of the Electronic-Spectra of Tris(Mu-Halo)Bis-(Triammineruthenium)(2+) Ions Using Resonance Raman-Spectroscopy. *Inorg. Chem.* **1990**, *29* (22), 4551−4556.

(47) Noctor, G. Metabolic signalling in defence and stress: the central roles of soluble redox couples. *Plant, Cell Environ.* **2006**, *29* (3), 409−425.

(48) Cushing, B. L.; Kolesnichenko, V. L.; O'Connor, C. J. Recent advances in the liquid-phase syntheses of inorganic nanoparticles. *Chem. Rev.* **2004**, *104* (9), 3893−3946.

(49) Webb, M. I.; Walsby, C. J. Control of ligand-exchange processes and the oxidation state of the antimetastatic Ru(III) complex NAMI-A by interactions with human serum albumin. *Dalton T* **2011**, *40* (6), 1322−1331.

(50) Lombardi, J. R.; Birke, R. L. A unified approach to surface-enhanced Raman spectroscopy. *J. Phys. Chem. C* **2008**, *112* (14), 5605−5617.

(51) Staffa, J. K.; Lorenz, L.; Stolarski, M.; Murgida, D. H.; Zebger, I.; Utesch, T.; Kozuch, J.; Hildebrandt, P. Determination of the Local Electric Field at Au/SAM Interfaces Using the Vibrational Stark Effect. *J. Phys. Chem. C* **2017**, *121* (40), 22274−22285.

(52) Lever, A. B. P. Electrochemical Parametrization of Metal-Complex Redox Potentials, Using the Ruthenium(III) Ruthenium(II) Couple to Generate a Ligand Electrochemical Series. *Inorg. Chem.* **1990**, *29* (6), 1271−1285.